Single-Crystal γ-MnS Nanowires Conformally Coated with Carbon

Juan Beltran-Huarac,*[†,‡] Oscar Resto,[‡] Jennifer Carpena-Nuñez,[‡] Wojciech M. Jadwisienczak,[§] Luis F. Fonseca,[†,‡] Brad R. Weiner,[†,‖] and Gerardo Morell[†,‡]

[†]Institute for Functional Nanomaterials, University of Puerto Rico, San Juan, Puerto Rico 00931, United States

[‡]Department of Physics and [‖]Department of Chemistry, University of Puerto Rico, San Juan, Puerto Rico 00936, United States

[§]School of Electrical Engineering and Computer Science, Ohio University, Athens, Ohio 45701, United States

ABSTRACT: We report for the first time the fabrication of single-crystal metastable manganese sulfide nanowires (γ-MnS NWs) conformally coated with graphitic carbon via chemical vapor deposition technique using a single-step route. Advanced spectroscopy and electron microscopy techniques were applied to elucidate the composition and structure of these NWs at the nanoscale, including Raman, XRD, SEM, HRTEM, EELS, EDS, and SAED. No evidence of α-MnS and β-MnS allotropes was found. The γ-MnS/C NWs have hexagonal cross-section and high aspect ratio (~1000) on a large scale. The mechanical properties of individual γ-MnS/C NWs were examined via in situ uniaxial compression tests in a TEM-AFM. The results show that γ-MnS/C NWs are brittle with a Young's modulus of 65 GPa. The growth mechanism proposed suggests that the bottom-up fabrication of γ-MnS/C NWs is governed by vapor-liquid-solid mechanism catalyzed by bimetallic Au−Ni nanoparticles. The electrochemical performance of γ-MnS/C NWs as an anode material in lithium-ion batteries indicates that they outperform the cycling stability of stable micro-sized α-MnS, with an initial capacity of 1036 mAh g^{-1} and a reversible capacity exceeding 503 mAh g^{-1} after 25 cycles. This research advances the integration of carbon materials and metal sulfide nanostructures, bringing forth new avenues for potential miniaturization strategies to fabricate 1D core/shell heterostructures with intriguing bifunctional properties that can be used as building blocks in nanodevices.
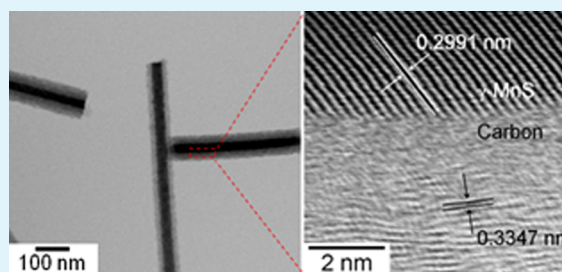
KEYWORDS: nanowires, lithium-ion battery, mechanical properties, MnS, core/shell

■ INTRODUCTION

Over the past few years, many efforts have been devoted to the fabrication and prospective technological applications of one-dimensional (1D) nanoscale building blocks, such as nanorods, nanowires (NWs), nanobelts, and nanotubes.[1−5] Transition-metal sulfide NWs have been applied to many distinct industrial areas including diluted magnetic semiconductor devices, lasers, single-electron transistors, flat panel displays, infrared windows, photovoltaic devices, sensors, biological labeling and diagnostics, and diodes.[6,7] Manganese sulfide (MnS) is a p-type semiconductor ($E_g \approx 3.2$ eV at room temperature) and crystallizes in three distinct phases: rock-salt (α-MnS), zinc-blende (β-MnS), and wurtzite (γ-MnS).[8] Metastable γ-MnS bulk does not exist in nature, but its synthesis in laboratory under unusual conditions shows that γ-MnS nanostructures exhibit unique chemical, electrical and magneto-optical properties superior to α-MnS.[9−12] These properties can be further tailored, which would render γ-MnS more appealing and suitable for various applications.

Some methods to grow γ-MnS hierarchical structures and microspheres have been published; however, there are very few reports on the fabrication of nanostructured γ-MnS.[13−21] These reports have failed to generate single-crystal NWs and lack convincing experimental support regarding the production of high-quality metastable γ-MnS NWs. Moreover, the reported γ-

MnS nanostructures suffer oxidation, deformation, corrosion, and contamination due to their high-chemical reactivity hampering their practical applications.[22] This standing problem has not been solved yet.

Core/shell 1D nanostructures have been widely used to encapsulate a highly reactive core within a different shell material in order to generate a physical barrier between the interior and the surrounding medium.[23] This enables core materials to be less sensitive to environmental changes, surface chemistry and photo-oxidation providing them an enhanced stability and a more efficient surface passivation.[24,25] For instance, the protection of zinc sulfide (ZnS) NWs against oxidation and decomposition has been successfully carried out by distinct shell materials, such as silicon dioxide (SiO$_2$) and boron nitride (BN).[26,27] Recently, many efforts have been made to fabricate the core/shell nanowires via single-step CVD method, particularly with carbon shell.[22,28] Moreover, the integration of carbon with metal sulfides to fabricate composites has enabled the formation of efficient electronic conducting frameworks.[29−31] These metal-sulfide/carbon nanostructures offer a large electrode/electrolyte interface for

charge-transfer reactions, which enhances the performance of electrochemical lithium-ion batteries (LIBs)[29] when employed as anode materials.

In order to fully utilize γ-MnS NWs in nanodevices, an effective sheath using a proper shell material is needed, analogous to ZnS NWs. We report here for the first time the fabrication of single-crystal γ-MnS NWs conformally coated with graphitic carbon via a chemical vapor deposition technique using a single-step, inexpensive and environmentally friendly route. The chemical, structural, mechanical, and electrochemical properties of these NWs are studied.

■ EXPERIMENTAL SECTION

Materials. All reagents used in this investigation, manganese chloride ($MnCl_2$), gold chloride ($AuCl_3$), nickel nano-powder, and sulfur powder, were analytical-grade reagents (> 99.999 %) from Sigma Aldrich, USA, and were directly used without any processing.

Fabrication of γ-MnS/C Nanowires. γ-MnS/C NWs were grown on (001)Si substrates, which were thoroughly cleaned with acetone and then dried with nitrogen. $AuCl_3$ was added to a saturated-Ni solution in isopropanol (1:1 wt %), and then this mixture was ultrasonicated for 30 min. This homogeneous solution was next dripped into the so-treated Si-substrate surfaces achieving a full and uniform cover, and heated up to evaporate the solvent and any remaining absorbate. The Au−Ni catalyst-covered Si substrates and $MnCl_2$ and sulfur powder were placed into a fused silica tube in a hot-wall horizontal furnace. The amounts of sulfur and $MnCl_2$ were adjusted in order to obtain a 1:3 Mn/S molar ratio. $MnCl_2$ was positioned in the middle of the furnace (hot zone), where the temperature (1273 K) was monitored; whereas the sulfur (down-stream) and the Si substrate (upstream) were placed at certain distance from $MnCl_2$ and kept at ∼673 and 1123 K, respectively (see diagram in Figure 1). The reaction tube was first evacuated down to
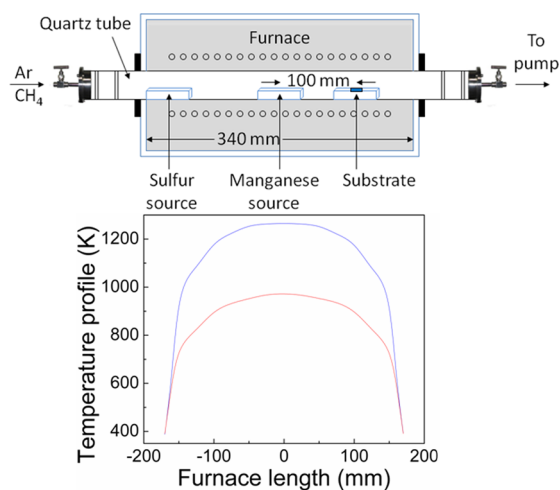
Figure 1. Depiction of apparatus (upper) and temperature profile (lower) of the hot-wall horizontal furnace for the fabrication of core/shell γ-MnS/C NWs.

465 mPa, heated to 1273 K, and filled to 46.5 Pa with a gas mixture having a constant Ar flow at 20 sccm and methane flow at 5 sccm. Hydrogen dilution was not required. After 1 h, the $MnCl_2$ and S were fully consumed, and the methane flow was turned off. After this point, the samples were further annealed for 1 h. The tube was left to cool spontaneously to room temperature. Only amorphous Mn−S−C NWs were obtained before the annealing process, as verified by SEM and TEM analyses (not shown). Moreover, in the absence of catalytic material, no γ-MnS/C NWs were obtained. The nanowires were transferred to a TEM grid upon carefully scratching the Si surface using a diamond tip for characterization and analyses.

Characterization. The crystalline structure of the samples was studied using an X-ray diffractometer (XRD), Model Siemens D5000 with Cu K_α radiation. Raman spectra were collected via a Jobin-Yvon T64000 spectrometer (instrumental error ∼1 cm^{-1}) with Ar-ion laser excitation (514.5 nm) and attached to an optical microscope with 80× resolution. The surface morphology, elemental composition and topography were analyzed using a JEOL JSM-7500F field-emission scanning electron microscope (FE-SEM) and a JEOL JEM-2200FS Cs-corrected high-resolution TEM (HRTEM). All the images were taken in scanning TEM (STEM) mode.

For in situ mechanical experiments, an AFM holder (Nanofactory Instruments AB, TEM-AFM) within a high-resolution TEM chamber was employed. The as-synthesized γ-MnS/C NWs were directly glued to a 250 μm thick Au wire with conductive silver epoxy and were then cured at room temperature for 24 h. The sample and force sensor (Nanofactory Instruments AB) were mounted in the TEM-AFM specimen holder. Rough alignment of the sample and AFM sensor was performed in air prior to insertion into the TEM chamber. After the selection of NWs (desired dimensions and orientations with respect to the force sensor), they were brought into contact by Z-height and sample position adjustment via a piezo-driven manipulation stage. Conditioning testing was first executed by aligning the displacement axis, optimizing the stress axis and pinning tightly the NW on the force sensor (avoiding any slippage). The mechanical measurements were registered by loading the selected NW (uniaxial compression) until the failure of the material was observed. The manipulation of the NW was recorded via TEM imaging simultaneous to the force data acquisition. Several γ-MnS/C NWs were tested following this procedure.

For electrochemical measurements, γ-MnS/C NWs were used as the working electrode material and Li-metal foil as counter and reference electrode. The electrode was fabricated by mixing active material (92 wt %) and polyvinylidene fluoride (PVDF) binder (8 wt %) in n-methyl pyrrolidone (NMP) solvent on Cu foil to form a homogeneous slurry. No conductive carbon black was employed. The slurry was then dried and pressed to enhance the conductivity. Coin cells were prepared in an Ar atmosphere inside a glove box (M. Braun, USA). The electrodes were separated inside the coin cell using a Celgard 2400 membrane. Lithium hexafluorophosphate dissolved in a mixture of ethylene carbonate (EC) and dimethyl carbonate (DMC) in (1:1, v/v) was used as the electrolyte. The charge-discharge curves were obtained using a Gamry Instruments potentiostat and PHE200 electrochemical software. They were done at a current density of 1000 mAg^{-1} and in the 0-3 V voltage range (scan rate of 0.2 mV/s).

■ RESULTS AND DISCUSSION

The XRD pattern of the as-synthesized MnS/C films is shown in Figure 2a. The diffraction peaks observed were indexed to the diffraction planes of hexagonal wurtzite MnS (γ-MnS) phase [(100), (002), (101), (102), (110), (103), (200), (112) and (201)] according to the JCPDS card, File No. 40-1289 and space group P63mc. Based on the peak positions, the α-MnS phase can be ruled out. However, three of the peak positions overlap with those of β-MnS (JCPDS No. 401288), whose presence cannot be discarded. The sharp peaks found and the absence of impurities in the diffractogram indicates that the metastable γ-MnS phase is of high crystalline quality and purity. An additional diffraction peak observed at around 25° corresponds to the (002) plane of graphitic carbon, indicating the formation of a γ-MnS/C hybrid material.

The γ-MnS/C films were also studied by Raman scattering spectroscopy (Figure 2b). The two well-pronounced high-frequency Raman bands were simulated using the damped harmonic oscillator phonon model (DHOPM).[32] From the simulation, the bands are determined to be at 1340.1 cm^{-1} and 1589.5 cm^{-1}, which correspond to the disorder-induced band of graphitic carbon (D band) and the bond stretching of all pairs of sp^2 carbon (G band), respectively.[32] From the simulation,
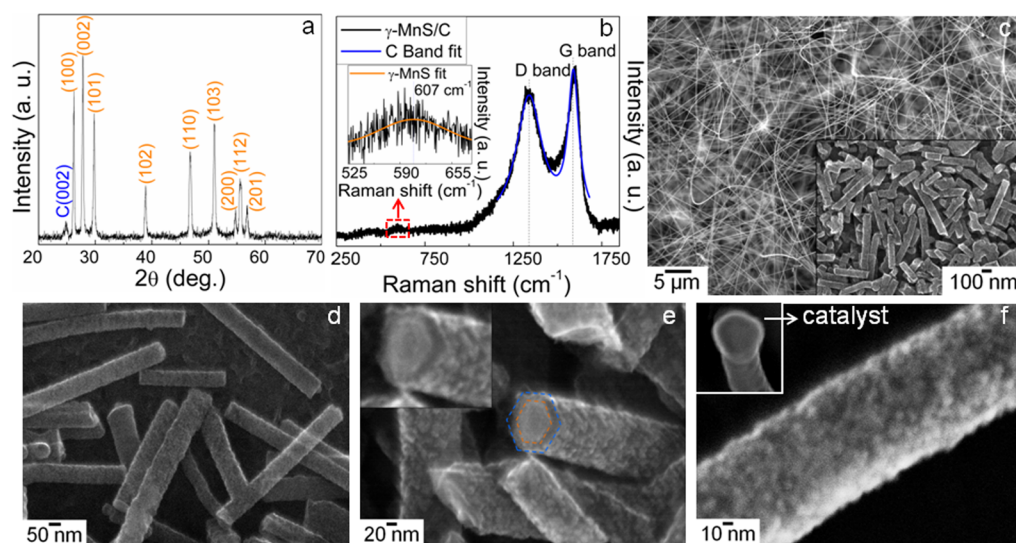
Figure 2. (a) XRD pattern, (b) micro-Raman spectrum, and (c−f) FE-SEM images of γ-MnS/C NWs. Blue solid line in b corresponds to the DHOPM fit (inset shows the fit of γ-MnS). Inset in c shows how the NWs look like after they were transferred to a TEM grid. Inset in e shows a close-up of an individual NW. Inset in f shows the catalyst at the end of a individual NW.

the ID/IG ratio is ∼0.76 and the bandwidths are ∼150 cm^{-1} (D band) and ∼62 cm^{-1} (G band). The ID/IG ratio <1 indicates a moderate degree of disorder in the graphitic phase. The low-frequency Raman mode centered at 607 cm^{-1} (see inset of Figure 2b) can be ascribed to scattering involving two magnon branches (2M) occurring in MnS.[33] The corresponding fit shows that this band is red-shifted by ∼8 cm^{-1} and broadened (FWHM ∼97 cm^{-1}) when compared to bulk MnS,[33] which indicates that the γ-MnS phase is under tensile stress developed during the growth process of the hybrid material. Note that this band is relatively weak because of the fact that the Raman spectrum was collected at room temperature, which is above the Néel temperature (∼90 K) for γ-MnS nanostructures.[34] Taken altogether, the Raman analysis indicates the formation of a γ-MnS/C hybrid material, consistent with the XRD analysis.

The FE-SEM images depicted in Figure 2c−f show γ-MnS/C at different magnifications. The γ-MnS/C films are a few micrometers thick and densely populated with spaghettilike NWs (Figure 2c). These γ-MnS/C NWs possess a high aspect ratio (AR) with diameters falling in the range of 60-100 nm and lengths over 100 μm. However, they break into smaller rods during manipulation and transfer to a TEM grid substantially reducing their AR (inset of Figure 2c). No sign of the catalytic material was found on the top end of individual γ-MnS/C NWs indicating that they grew with the catalyst at the base (i.e., base-growth model[32,35]). Figure 2d shows that γ-MnS/C NWs consist of a core/shell structure with hexagonal cross-section, or hexagonal NWs uniformly covered by a smooth shell layer. These features were highlighted by overlaying two concentric hexagons on the image of Figure 2e (see also inset therein): an orange hexagon for the core material and a larger blue hexagon for the shell material. The perfectly radial cuts suggest that γ-MnS/C NWs were subject to shear stress during transfer.

The HRTEM images, electron energy loss spectra (EELS) and energy-dispersive X-ray spectroscopy (EDS) line-scans, and selected area electron diffraction (SAED) pattern of γ-MnS/C NWs are depicted in Figure 3. The conformal coating of the shell material (light) onto the core material (dark) is evident from Figure 3a. The outer diameter of the NWs is around 60−100 nm, whereas the inner diameters are between 20 and 50
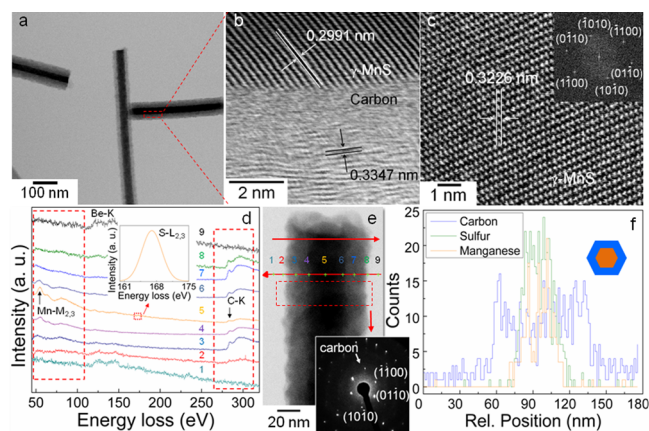
Figure 3. (a) HRTEM images of representative γ-MnS/C NWs. Closer views at (b) the interface and (e, f) inside single-crystal γ-MnS of γ-MnS/C NW. The inset in c shows the FFT image corresponding to c. (d) EELS spectra and (f) EDS profile line-scanned from the region shown in e corresponding to an individual γ-MnS/C NW. Inset in d shows a zoom of the S L2,3-shell edge. The inset in e shows the SAED pattern of an individual γ-MnS/C NW.

nm. The width of the interface between the shell and core was estimated to be <0.5 nm (see Figure 3b at lattice-resolved resolution). This indicates that such an interface is not only thin, but also smooth and abrupt. Hence, this method provides an efficient route to develop 1D core/shell heterostructures with low degree of interdiffusion between the core and shell material, even after harsh annealing treatments. Figure 3b also enables us to distinguish the lattice fringes of the constituent phases. The d-spacings found are $d_{100} = 0.3347$ and $d_{101} = 0.2991$ nm, characteristic of graphitic carbon and wurtzite MnS, respectively.[36] The high degree of crystallinity in both phases is consistent with the XRD and Raman analyses. A closer view of the core material (see Figure 3c) shows a regular atomically-resolved arrangement with an interplanar spacing of 0.3226 nm perpendicular to the nanowire axis ([0002] direction),[15] which further confirms the formation of γ-MnS. A closer look at the γ-MnS crystalline structure shows that the individual hexagons of

1182

dx.doi.org/10.1021/am404746k | ACS Appl. Mater. Interfaces 2014, 6, 1180−1186

the structural arrangement are slightly distorted, consistent with the tensile strain indicated by the Raman analysis. In addition, the indexation by means of the fast Fourier transform (FFT) is consistent with the hexagonal structure of γ-MnS (see inset of Figure 3c).

To clearly establish the nature of the carbon material coating the γ-MnS NWs, we performed EELS operated in STEM mode. Line-scanned EELS spectra are depicted in Figure 3d, which were carried out on the region shown in Figures 3e. The EELS spectra show the C edge π^* transition at ~285 eV and the σ^* transition at ~292 eV, which correspond to sp^2 C, strong at the borders and fading towards the center of the NWs. Two more bands peaking at ~165 and 55 eV were observed (see Figure 3g and inset therein) and attributed to the S $L_{2,3}$ and the low-loss Mn $M_{2,3}$ transitions, respectively. They show that S and Mn are strong in the core and fade at the border of the NWs. Beryllium K-shell (~111 eV) ionization edge was also detected beyond the outer borders of the NWs, which is ascribed to the specimen sample holder. These data further evidence at atomic resolution that the NWs possess a well-defined core/shell structure having γ-MnS at the center and sp^2-bonded carbon on the borders, which correlates with the Raman analyses.

The single-crystal nature of γ-MnS is evidenced of the SAED pattern (carried out on the region shown in Figures 3e and operated in TEM mode), whose indexation (see inset of Figure 3e) agrees with that obtained by XRD. In addition, the EDS (operated in STEM mode) line-scans (Figure 3f) shows that the shell (~20 nm thick) consists of carbon and the core (~40 nm) consists of Mn and S. These thicknesses correlate well with the average values estimated from the HRTEM images. We also performed EDS elemental mappings of the NWs (not shown here) to reveal the overall distribution of C, S, and Mn. The EDS mappings were carried out on the same but broader region tested by EELS. They show strong signals of Mn and S at the core, and C all around the NWs, consistent with the EELS data.

Thus, considered altogether, our findings show that core/shell NWs were synthesized consisting of a core made of single-crystal γ-MnS along the [0002] direction and a shell made of graphitic carbon. Analogous results have been previously reported[22,37,38] for carbon-coated ZnS NWs, apatite NWs sheathed in graphitic shells, and In−Sn NWs sheathed in carbon nanotubes.

We have conducted a series of uniaxial compression experiments on individual γ-MnS/C NWs via in situ TEM-AFM in order to shed light on their mechanical properties. The TEM-AFM holder setup employed is shown in Figure 4a, which was placed inside the TEM chamber. Figure 4b shows the TEM image of an individual γ-MnS/C NW mounted on Cu wire. The uniaxial compression tests were done by moving the piezo-driven stage forward and keeping the Au wire stationary. TEM images of uniaxial compression tests before and after fracture and the corresponding force-displacement (F/D) curve are depicted in Figures 4c−e. It was found that individual γ-MnS/C NWs experienced a weak plastic deformation. The NWs fractured in a brittle mode at a critical force of 1330 nN, as evidenced in the F/D curve, which exhibited a rapid load release along the Z axis. The fracture edge is shown in inset of Figure 4e. The Young's modulus was calculated using Euler's relation as follows

$$E = \frac{64 F_{\text{Euter}}(kl)^2}{\pi^3 d^4} \tag{1}$$
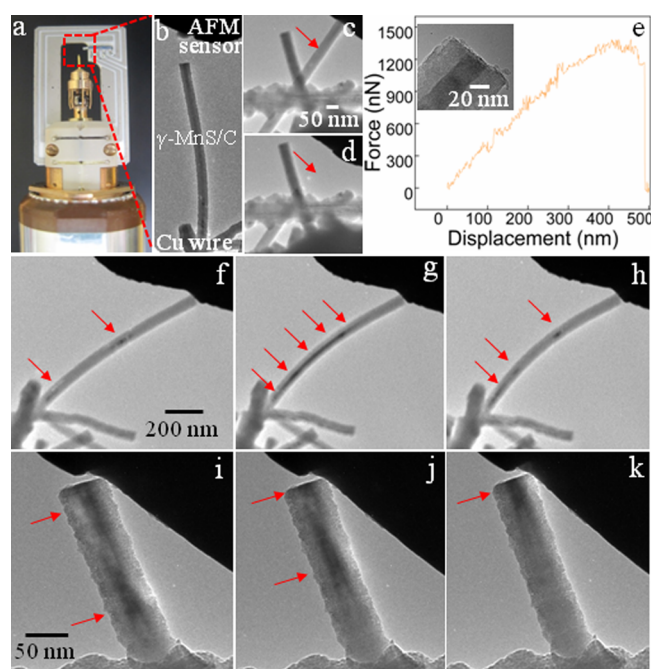
Figure 4. (a) Optical image of the TEM-AFM holder setup and (b) TEM-AFM setup as viewed under the TEM. TEM images of axial compression tests of individual γ-MnS/C NWs (c) before and (d) after brittle fracture and the corresponding F/D curve e. Inset in e shows the fracture edge. Sequence of TEM images showing strain displacement mainly along the core material as the NWs were subject to (f−h) bending and (i−k) uniaxial stress.

where F_{Euler}, k, l, and d represent the applied load (determined from the F/D curve, average force at the plateau zone), the effective length factor ($k = 0.699$ for one end pinned and the other fixed), the length ($l \approx 1$ μm ascertained from TEM projection) and diameter ($d \approx 68$ nm) of the NW, respectively. This relation considers the NWs as perfect homogeneous solid wires in which Hooke's law holds. We obtained the value of 65 GPa for the Young's modulus of γ-MnS/C NW. Although there are no reports of MnS Young's modulus, this value is one order of magnitude lower than that of bulk wurtzite ZnS ($E = 128$ GPa).[39−41] The reduction of the elastic modulus in sulfide-based NWs (compared to their bulk counterpart) is presumably ascribed to the higher surface area of NWs. Surface atoms are less constrained (compared to atoms bound to the lattice), thus rendering the NWs easier to deform in the plastic regime and feasible to reduce the elastic modulus.[42,43] Likewise, the calculated Young's modulus is comparable to those of highly crystalline 1D ZnS building blocks,[1−5] such as wurtzite ZnS NWs ($E = 52$ GPa), ZnS nanofilaments ($E = 36−64$ GPa) and ZnS nanobelts ($E = 36$ GPa).[42,43] Nonetheless, it is three orders of magnitude lower than that of the carbon fibers, which indicates that the modulus is dominated by the core material.

To corroborate the small contribution of the carbon shell in the elastic modulus, γ-MnS/C NWs were subject to bending and uniaxial stress below the fracture regime, a sequence of TEM images are depicted in Figure 4f−k. The stress can be clearly identified from TEM phase contrast change as indicated by the red arrows. It was observed that as the compression increases, the strain travels mainly along the core material and to a lower degree along the shell material. This indicates that the core carries the load, whereas the shell relieves the load minimally, consistent with the fact that γ-MnS possesses a

higher degree of crystallinity than the carbon coating, which consists of graphitic and amorphous carbon, as discussed above. In fact, the failure along the cleavage planes is a clear indicator that the failure threshold is dictated by the core in the hybrid material. Therefore, the brittle fracture occurred perpendicularly to the growth direction, i.e., the [0002] direction of the γ-MnS/C NWs, which is consistent with our HRTEM studies. Hence, our method can provide 1D core/shell NWs exhibiting stress-free carbon shells, which is critical for shock-resistant semiconductor technology.

The synthesis of core/shell γ-MnS/C NWs achieved by the single-step CVD method hereby described involves complex physicochemical processes beyond the scope of this work. Nevertheless, we highlight some qualitative aspects of the underlying vapor−liquid−solid (VLS) growth mechanism.[44−50] At the growth temperature of 1123 K, elemental Au and Ni nanoparticulate form bimetallic Au−Ni alloy droplets (AADs),[51−57] which exhibit a synergistic effect of high catalytic activity for sulfides and hydrocarbons.[46,48] At the liquid−solid interface of supersaturated AADs, the MnS synthesis reaction takes place

$$MnCl_2 + 3S \xrightarrow{\Delta H} MnS + S_2Cl_2 \qquad (2)$$
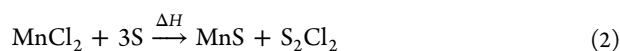
Similarly, hydrogen abstraction reactions of CH_x species take place at the AADs, leading to the formation of graphitic carbon. The net effect is the formation of amorphous Mn−S−C NWs with the AADs at base. Upon subsequent annealing, the amorphous Mn−S−C NWs undergo crystallization of the γ-MnS accompanied by massive precipitation of graphitic C to the surface, giving rise to the γ-MnS/C NWs, as shown in Figure 5.
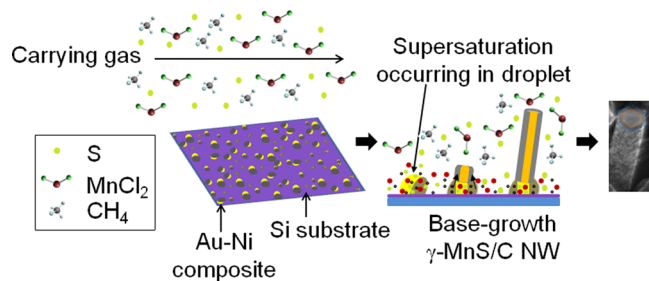
Figure 5. Illustration of the VLS mechanism for the synthesis of core/shell γ-MnS/C NWs.

We have also evaluated the electrochemical properties of core/shell γ-MnS/C NWs as a potential and alternative anode material for LIBs for the first time. Charge−discharge experiments were carried out in coin cells with γ-MnS/C NWs as the anode material. The corresponding charge−discharge curves are depicted in Figure 6. Discharge capacities of 1036 and 747 mAh g^{-1} are obtained for the first and second cycles, respectively. The first discharge capacity found is higher than that obtained for the first discharge capacity (878 mAh g^{-1}) of coral-like α-MnS composites with N-doped carbon.[58] These values also resulted to be comparable to single-crystal MnS microboxes[59] (1117 and 759 mAh g^{-1} first and second discharge capacities), and lower than α-MnS submicrocrystals[60] (1327 and 804 mAh g^{-1}, respectively). The reduction of charge capacity after each charge−discharge cycle indicates that irreversible structural changes took place during Li alloying, similar to those previously reported for α-MnS[58−60] and for
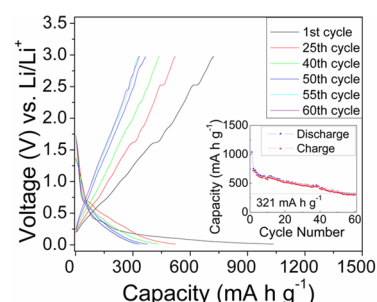
Figure 6. Charge−discharge voltage profiles and cycling performance (inset) of core/shell γ-MnS/C NWs employed as anode material.

composites consisting of metal sulfides and carbon.[61−63] From the second cycle onwards, it was also observed that γ-MnS/C NWs show remarkable cyclic capacity retention (67%) with a stable capacity of ∼503 mAh g^{-1} (higher than the theoretical capacity of graphite, 372 mAh g^{-1}) at the end of 25 charge−discharge cycles. After 60 cycles, this hybrid material still retained a reversible capacity exceeding 321 mAh g^{-1}, which is comparable to that found by Zhang et al.[59] working on porous MnS microcubes (340 mAh g^{-1} after 100 cycles), and lower than those previously reported for single-crystal MnS microboxes[59] (495 mAh g^{-1} after 100 cycles), α-MnS submicrocrystals[60] (587 mAh g^{-1} after 20 cycles), and coral-like α-MnS composites with N-doped carbon[58] (699 mAh g^{-1} after 400 cycles). This result can be ascribed to: (a) the nanoscale size of γ-MnS/C that reduces the Li diffusion length and increases the surface-to-volume ratio, thus improving their capability to accept Li ions, and (b) their good crystalline quality that enhances their ability to sustain reversible charge-discharge cycling.

Only a few reports on the electrochemical properties of stable micro-sized MnS have appeared in the literature (no report on metastable MnS nanostructures). This might be due to the fact that commercial MnS anodes exhibit poor capacity ∼50 mAh g^{-1} after four cycles.[58] Even though the theoretical capacity of MnS is 616 mAh g^{-1}, the initial capacity of commercial MnS falls off severely over cycling. In general, metal sulfides do not exhibit good charge cycling stability. Nonetheless, our preliminary results suggest that metastable γ-MnS NWs conformally coated by graphitic carbon show improved capacity and cycling as compared to commercial MnS. This performance can be attributed to the presence of highly conducting carbon (which enables the formation of a large electrode/electrolyte interface for the charge-discharge reaction[61−63]), the absence of disruptive agglomerative binders, homogeneous electrochemical accessibility, large contact area between the active material and electrolyte (which facilitates the Li$^+$ insertion/extraction), and highly crystalline nanowire morphology. Moreover, the carbon coating generates more active zones for the electrochemical reaction and impedes the decomposition of polysulfide as the conversion reaction of sulfides is occurring.[58] Notice that the carbon coating does not prevent Li ions from reaching the inner γ-MnS core as it is thinner than the Li-ion diffusion length.[64]

■ CONCLUSIONS

We have developed a straightforward synthesis method to produce high-quality single-crystal core/shell γ-MnS/C NWs by a single-step CVD route. This method does not require the use of expensive and highly-flammable hydrogen gas as

precursor, employs low synthesis temperatures (as compared to traditional thermal evaporation techniques ~1450 K), and is scalable for mass production. In this study, the big challenge of MnS oxidation was overcome by conformally coating the γ-MnS NWs with a protective graphitic carbon shell. During the VLS synthesis process, the AADs promote the catalyzed growth of smooth γ-MnS/C NWs by the base-growth mode. As an anode material, our findings indicate that γ-MnS/C NWs exhibit remarkable capacity and good cycling performance for LIBs. This study represents a step ahead in the efforts to integrate not only oxides but also metal sulfides with carbon into 1D core/shell building blocks. This breakthrough advances novel methods to fabricate sulfide-based electrode materials. Furthermore, it can lead to the fabrication of 1D core/shell NWs exhibiting stress-free carbon shells, which is critical for shock-resistant semiconductor technology.

■ AUTHOR INFORMATION

Corresponding Author
*E-mail: baristary26@gmail.com.

Notes
The authors declare no competing financial interest.

■ ACKNOWLEDGMENTS

■ REFERENCES

(1) Xia, Y.; Yang, P.; Sun, Y.; Wu, Y.; Mayers, B.; Gates, B.; Yin, Y.; Kim, F.; Yan, H. *Adv. Mater.* **2003**, *15*, 353−389.
(2) Deng, Z.; Tong, L.; Flores, M.; Lin, S.; Cheng, J.; Yan, H.; Liu, Y. *J. Am. Chem. Soc.* **2011**, *133*, 5389−5396.
(3) Duan, X.; Huang, Y.; Cui, Y.; Wang, J.; Lieber, C. M. *Nature* **2001**, *409*, 66−69.
(4) Pan, Z. W.; Dai, Z. R.; Wang, Z. L. *Science* **2001**, *291*, 1947−1949.
(5) Chopra, N. G.; Luyken, R. J.; Cherrey, K.; Crespi, V. H.; Cohen, M. L.; Louie, S. G.; Zettl, A. *Science* **1995**, *269*, 966−967.
(6) Ge, J.; Wang, J.; Zhang, H.; Li, Y. *Chem.—Eur. J.* **2004**, *10*, 3525−3530.
(7) Zhang, F.; Wong, S. S. *Chem. Mater.* **2009**, *21*, 4541−4554.
(8) Kennedy, S. W.; Harris, K.; Summerville, E. *J. Solid State Chem.* **1980**, *31*, 355−359.
(9) Yang, X.; Wang, Y.; Wang, K.; Sui, Y.; Zhang, M.; Li, B.; Ma, Y.; Liu, B.; Zou, G.; Zou, B. *J. Phys. Chem. C* **2012**, *116*, 3292−3297.
(10) Biswas, S.; Kar, S.; Chaudhuri, S. *Mater. Sci. Eng. B* **2007**, *142*, 69−77.
(11) Zhang, P.; Zeng, Q.; He, X.; Tang, H.; Huang, K. *J. Cryst. Growth* **2008**, *310*, 4268−4272.
(12) Ren, Y.; Gao, L.; Sun, J.; Liu, Y.; Xie, X. *Ceram. Int.* **2012**, *38*, 875−881.
(13) Yang, X.; Wang, Y.; Sui, Y.; Huang, X.; Cui, T.; Wang, C.; Liu, B.; Zou, G.; Zou, B. *Langmuir* **2012**, *28*, 17811−17816.
(14) Lei, S.; Tang, K.; Yang, Q.; Zheng, H. *Eur. J. Inorg. Chem.* **2005**, *2005*, 4124−4128.
(15) Ma, W.; Chen, G.; Zhang, D.; Zhu, J.; Qiu, G.; Liu, X. *Mater. Res. Bull.* **2012**, *47*, 2182−2187.
(16) Wang, S.; Li, K.; Zhai, R.; Wang, H.; Hou, Y.; Yan, H. *Mater. Chem. Phys.* **2005**, *91*, 298−300.
(17) Lu, J.; Qi, P.; Peng, Y.; Meng, Z.; Yang, Z.; Yu, W.; Qian, Y. *Chem. Mater.* **2001**, *13*, 2169−2172.
(18) Ge, J.; Li, Y. *Chem. Commun.* **2003**, 2498−2499.
(19) Zhang, C.; Tao, F.; Liu, G. Q.; Yao, L. Z.; Cai, W. L. *Mater. Lett.* **2007**, *62*, 246−248.
(20) Jun, Y.; Jung, Y.; Cheon, J. *J. Am. Chem. Soc.* **2002**, *124*, 615−619.
(21) Zheng, Y.; Cheng, Y.; Wang, Y.; Zhou, L.; Bao, F.; Jia, C. *J. Phys. Chem. B* **2006**, *110*, 8284−8288.
(22) Shen, G.; Bando, Y.; Golberg, D. *J. Phys. Chem. B* **2006**, *110*, 20777−20780.
(23) Reiss, P.; Protiere, M.; Li, L. *Small* **2009**, *5*, 154−168.
(24) Wang, Z.; Guo, R.; Li, G.; Ding, L.; Ou, Y.; Tong, Y. *RSC Adv.* **2011**, *1*, 48−51.
(25) Xie, S.; Lu, X.; Zhai, T.; Gan, J.; Li, W.; Xu, M.; Yu, M.; Zhang, Y.; Tong, Y. *Langmuir* **2012**, *28*, 10558−10564.
(26) Zhu, Y.; Bando, Y.; Yin, L. *Adv. Mater.* **2004**, *16*, 331−334.
(27) Li, Y.; Ye, C.; Fang, X.; Yang, L.; Xiao, Y.; Zhang, L. *Nanotechnology* **2005**, *16*, 501−504.
(28) Li, Q.; Liu, R.; Liu, B.; Li, D.; Zou, B.; Cui, T.; Liu, B. *J. Mater. Res.* **2013**, *28*, 449−453.
(29) Li, Y.; Qiao, Y.; Zhang, W.; Li, Z.; Hu, X.; Yuan, L.; Huang, Y. *J. Mater. Chem.* **2012**, *22*, 24026−24033.
(30) Luo, B.; Fang, Y.; Wang, B.; Zhou, J.; Song, H.; Shi, L. *Energy Environ. Sci.* **2012**, *5*, 5226−5230.
(31) Chang, K.; Chen, W. *ACS Nano* **2011**, *5*, 4720−4728.
(32) Beltran-Huarac, J.; Carpena-Nuñez, J.; Barrionuevo, D.; Mendoza, F.; Katiyar, R. S.; Fonseca, L. F.; Weiner, B. R.; Morell, G. *Carbon* **2013**, *65*, 252−260.
(33) Chou, H-h.; Fan, H. Y. *Phys. Rev. B: Condens. Matter Mater. Phys.* **1976**, *13*, 3924−3938.
(34) Banewicz, J.; Lindsay, R. *Phys. Rev.* **1956**, *104*, 318−320.
(35) Fan, H. J.; Lee, W.; Hauschild, R.; Alexe, M.; Rhun, G. L.; Scholz, R.; Dadgar, A.; Nielsch, K.; Kalt, H.; Krost, A.; Zacharias, M.; Gosele, U. *Small* **2006**, *2*, 561−568.
(36) Dhanam, M.; Kavitha, B.; Shanmugapriya, M. *Chalcogenide. Lett.* **2009**, *6*, 541−547.
(37) Jeong, N.; Cha, M.; Park, Y. C.; Lee, K. M.; Lee, J. H.; Park, B. C.; Lee, J. *ACS Nano* **2013**, *7*, 5711−5723.
(38) Jeong, N.; Yeo, J-g. *Nanotechnology* **2012**, *23*, 285604.
(39) Mandal, T.; Maiti, P. K.; Dasgupta, C. *Phys. Rev. B: Condens. Matter Mater. Phys.* **2012**, *86*, 024101.
(40) Harris, D. C.; Boronowski, M.; Henneman, L.; LaCroix, L.; Wilson, C.; Kurzius, S.; Burns, B.; Kitagawa, K.; Gembarovic, J.; Goodrich, S. M.; Staats, C.; Mecholsky, J. J., Jr. *Opt. Eng.* **2008**, *47*, 114001.
(41) Cline, C. F.; Dunegan, H. L.; Henderson, G. W. *J. Appl. Phys.* **1967**, *38*, 1944−1948.
(42) Xiong, Q.; Duarte, N.; Tadigadapa, S.; Eklund, P. C. *Nano Lett.* **2006**, *6*, 1904−1909.
(43) Li, X.; Wang, X.; Xiong, Q.; Eklund, P. C. *Nano Lett.* **2005**, *5*, 1982−1986.
(44) Dutra, A. T.; Ferrandini, P. L.; Costa, C. A. R.; Gonçalves, M. C.; Caram, R. *J. Alloys Compd.* **2005**, *399*, 202−207.
(45) Duan, X.; Lieber, C. M. *Adv. Mater.* **2000**, *12*, 298−302.
(46) Wang, X.; Song, J.; Summers, C. J.; Ryou, J. H.; Li, P.; Dupuis, R. D.; Wang, Z. L. *J. Phys. Chem.* **2006**, *110*, 7720−7724.
(47) Popovitz-Biro, R.; Kretinin, A.; Huth, P. V.; Shtrikman, H. *Cryst. Growth Des.* **2011**, *11*, 3858−3865.
(48) Lauhon, L. J.; Gudiksen, M. S.; Wang, D.; Lieber, C. M. *Nature* **2002**, *420*, 57−61.
(49) Meng, X. Q.; Zhao, D. X.; Zhang, J. Y.; Shen, D. Z.; Lu, Y. M.; Liu, Y. C.; Fan, X. M. *Chem. Phys. Lett.* **2005**, *407*, 91−94.
(50) Kolasinski, K. W. *Curr. Opin. Solid State Mater. Sci.* **2006**, *10*, 182−191.

(51) Kim, C.-C.; Wang, C.; Yang, Y.-C.; Hwu, Y.; Seol, S.-K.; Kwon, Y.-B.; Chen, C.-H.; Liou, H.-W.; Lin, H.-M.; Margaritondo, G.; Ge, J.-H. *Mater. Chem. Phys.* **2006**, *100*, 292−295.

(52) Rousset, J. L.; Santos Aires, F. J. C.; Sekhar, B. R.; Melinon, P.; Prevel, B.; Pellarin, M. *J. Phys. Chem. B* **2000**, *104*, 5430−5435.

(53) Nikolaev, S. A.; Yu. Vasil'kov, A.; Smirnov, V. V.; Tyurina, L. A. *Kinet. Catal.* **2005**, *46*, 867−872.

(54) Smirnov, V. V.; Lanin, S. N.; Yu. Vasil'kov, A.; Nikolaev, S. A.; Murav'era, G. P.; Tyurina, L. A.; Vlasenko, E. V. *Russ. Chem. Bull. Int. Ed.* **2005**, *43*, 2286−2289.

(55) Naumkim, A. V.; Yu. Vasil'kov, A.; Volkov, I. O.; Smirnov, V. V.; Nikolaev, S. A. *Inorg. Mater.* **2007**, *43*, 381−385.

(56) Pung, S.-Y.; Choy, K.-L.; Hou, X. *J. Cryst. Growth* **2010**, *312*, 2049−2055.

(57) Goede, O.; Heimbrodt, W.; Weinhold, V.; Schnürer, E.; Eberle, H. G. *Phys. Status Solidi B* **1987**, *143*, 511−518.

(58) Liu, Y.; Qiao, Y.; Zhang, W.-X.; Li, Z.; Hu, X.-L.; Yuan, L.-X.; Huang, Y.-H. *J. Mater. Chem.* **2012**, *22*, 24026−24033.

(59) Zhang, L.; Zhou, L.; Wu, H. B.; Xu, R; Lou, X. W. *Angew. Chem., Int. Ed.* **2012**, *51*, 7267−7270.

(60) Zhang, N.; Yi, R.; Wang, Z.; Shi, R.; Wang, H.; Qiu, G.; Liu, X. *Mater. Chem. Phys.* **2008**, *111*, 13−16.

(61) Xu, C.; Zeng, Y.; Rui, X.; Xiao, N.; Zhu, J.; Zhang, W.; Chen, J.; Liu, W.; Tan, H.; Hng, H. H.; Yan, Q. *ACS Nano* **2012**, *6*, 4713−4721.

(62) Chang, K.; Chen, W. *ACS Nano* **2011**, *5*, 4720−4728.

(63) Luo, B.; Fang, Y.; Wang, B.; Zhou, J.; Song, H.; Zhi, L. *Energy Environ. Sci.* **2012**, *5*, 5226−5230.

(64) Claye, A. S.; Fischer, J. E.; Huffman, C. B.; Rinzler, A. G.; Smalley, R. E. *J. Electrochem. Soc.* **2000**, *147*, 2845−2852.